

Article

Numerical Investigation of High-Purity Entangled Photon-Pair Generation in $\text{Ba}_3\text{Mg}_3(\text{BO}_3)_3\text{F}_3$ Crystals

Donghwa Lee, Ilhwan Kim and Kwang Jo Lee * 

Department of Applied Physics, Institute of Natural Science, Kyung Hee University, Yongin-si 17104, Korea; fairytale095@gmail.com (D.L.); dlfgkhs383@gmail.com (I.K.)

* Correspondence: kjlee88@khu.ac.kr

Received: 31 October 2020; Accepted: 18 December 2020; Published: 21 December 2020



Abstract: We investigate the high-purity entangled photon pair generation in a recently developed borate crystal, $\text{Ba}_3\text{Mg}_3(\text{BO}_3)_3\text{F}_3$. The technique is based on the spontaneous parametric down-conversion under the extended phase matching (EPM), where the phase matching and the group velocity matching between the interacting photons are satisfied simultaneously in bulk crystals with point symmetry of orthorhombic $mm2$ (thus showing biaxial birefringence). We will discuss all the theoretical aspects required for the generation of photon pairs in $mm2$ biaxial crystals, which are much more complex than the cases of uniaxial crystals (e.g., β - BaB_2O_4 and LiNbO_3) and periodically poled crystals that are widely used in the field. Our study includes theoretical and numerical investigations of two types of EPM and their corresponding effective nonlinearities and spatial walk-offs. The results show that two types of EPM are satisfied over the specific range in the direction of pump wave vector, corresponding to its spectral ranges of 876.15–1052.77 nm for Type I and 883.92–914.33 nm for Type II. The joint spectral analyses show that photon-pairs can be generated with high purities of 0.997 with a proper pump filtering (for Type II), and 0.833 even without pump filtering (for Type I).

Keywords: parametric down-conversion; photon-pair generation; extended phase matching; borate crystals

1. Introduction

Photon-pair sources based on spontaneous parametric down-conversion (SPDC) in nonlinear optic $\chi^{(2)}$ crystals are practical tools for experimental demonstrations of quantum metrology, quantum teleportation, quantum communication, and entanglement-based cryptography [1]. Various crystal platforms (e.g., β -barium borate (β - BaB_2O_4 or BBO), potassium dihydrogen phosphate (KH_2PO_4 or KDP), bismuth triborate (BiB_3O_6 or BiBO), and several periodically poled (PP) ferroelectric crystals, including lithium niobite (LiNbO_3 or LN) and potassium titanyl phosphate (KTiOPO_4 or KTP)) have been used for the SPDC based photon-pair sources since the first experimental demonstration using an ammonium dihydrogen phosphate ($\text{NH}_4\text{H}_2\text{PO}_4$ or ADP) crystal [2–9]. In particular, the pulsed pump SPDC source with the PPKTP Sagnac-loop configuration is known as a suitable platform for constructing practical quantum photonic networks, as it is advantageous for generating entangled photon pairs in the communication band [10–12]. Nevertheless, photon-pair generation using borate crystals such as BBO and BiBO in the visible range is still attractive due to the feasibility of realizing multi-photon entanglement, as well as the spectral preference of single-photon detection efficiency [7]. Since both physical and optical properties of borate crystals (e.g., hygroscopicity, transparency, birefringence, nonlinearity, and various causes of optical damage) generally depend on their crystal structures, it is always worthwhile to find another new borate crystal candidate to provide diversity and flexibility for SPDC-based quantum research [13].

Recently Mutailipu et al. reported a new borate crystal, $\text{Ba}_3\text{Mg}_3(\text{BO}_3)_3\text{F}_3$ (or BMBF) that has two types of polymorphs: orthorhombic and hexagonal crystal systems, respectively [14]. Of these two, the orthorhombic BMBF (the mm2 point symmetry, $Pna2_1$) exhibits a large laser damage threshold ($\sim 6.2 \text{ GW/cm}^2$), a deep-UV cutoff edge ($\lambda \sim 184 \text{ nm}$), a weak anisotropic thermal expansion, and the insolubility in water (i.e., the non-hygroscopicity unlike the BBO). These optical properties could be comparable or superior to that of commercial BBO. Second harmonic generation in a $Pna2_1$ -BMBF crystal was briefly discussed in [14], but since the BMBF is a newly developed crystal, no further nonlinear optical applications have been studied yet. Therefore, it is timely to investigate the usefulness of $Pna2_1$ -BMBF as another suitable candidate for the generation of entangled photon pairs.

In this paper, we theoretically and numerically investigate the SPDC properties of $Pna2_1$ -BMBF for application as an entangled photon-pair source. In Section 2, we theoretically describe two types of phase matching (PM) for the SPDC in a $Pna2_1$ -BMBF, i.e., Type I and Type II, where an input single photon (pump) with a frequency of 2ω generates a pair of photons (signal and idler) with identical frequencies of ω that are parallel (for Type I) or orthogonally (for Type II) polarized to each other. Then we discuss the group velocity (GV) matching between the interacting photon pulses, the effective nonlinearity in terms of d_{eff} coefficient, and the spatial walk-off for the given wave vectors, followed by a theoretical brief of the biphoton joint spectrum and spectral purity. Section 3 is devoted to discussing numerical simulation results, showing that the PM and GV matching conditions can be satisfied simultaneously over a specific range in the direction of pump wave vector. Thus, by sweeping the wave vector in this range, the resonant wavelength of pump that produces pure biphoton-states can be adjusted from 876.15 nm to 1052.77 nm for Type I and from 883.92 nm to 914.33 nm for Type II.

Here, we note that this condition is comparable to the extended phase matching (EPM) defined by Giovannetti et al. [15,16]. However, in Refs. [15,16], the simultaneous achievement of GV matching and quasi-phase matching (QPM) in a PP ferroelectric crystal is defined as the EPM, and in this case, the EPM can be satisfied only at one pump wavelength (and only one pump wave vector). In contrast, to the best of our knowledge, we report for the first time that the EPM can be achieved in the PM in a bulk mm2-biaxial crystal, as well as the QPM case in a PP crystal. In addition, we will also show that, in mm2-biaxial crystals, the EPM can be satisfied in a wide wavelength region (and in the specific range in the direction of pump wave vector), which is also contrasted with the cases of the uniaxial crystals in Refs. [2,3]. Of course, the spatial walk-off between the interacting beams occurs in our scheme, but this can be overcome by increasing the pump beam size. A larger pump beam window can be readily obtained by using thicker bulk crystals. In contrast, for the EPM using PP crystals, the crystal thickness (and the pump beam window) is limited by the maximum voltage that can be applied to the crystal during the periodic poling process. Since dielectric crystals are generally electrically conductive to some extent, if the voltage value required for the periodic poling exceeds the limit, the crystal burns and breaks during the fabrication process. In reality, the thickness of commercially available PPKTPs is about 0.5 mm [17]. Compared to the previous EPM case, our scheme has the advantage that it can use a large beam window if necessary, does not require post-processing of crystals such as periodic polling, and has a wide wavelength range (several tens of nanometers) that satisfies the EPM. In contrast, for the EPM cases reported so far, the SPDC has only one resonant wavelength [16,18–20].

Next, we will discuss the numerical simulation results of the effective nonlinearity (d_{eff}) and the spatial walk-off under the EPM, followed by the joint spectral analyses including the spectral purities calculated for several cases showing the largest nonlinearities. The results show that the calculated joint spectral amplitude (JSA) has a circular shape for Type II, and that photon-pairs can be generated with a high purity of 0.997 with a proper pump filtering. For Type I, the JSA shows a localized shape over a specific wavelength range even without pump filtering, and its purity is calculated as 0.833. Finally, the paper is summarized in Section 4.

2. Material and Theories

A $Pna2_1$ -BMBF has a point symmetry of orthorhombic $mm2$, and exhibits biaxial birefringence. The crystallographic axes of $Pna2_1$ -BMBF are all perpendicular to each other as shown in Figure 1a, and the lattice constants are $a = 0.80740$ nm, $b = 1.53072$ nm, and $c = 0.88218$ nm [14]. Since Mutailipu et al.'s study, the relations between the crystallographic axes and their optic axes are defined as $x = c$, $y = b$, and $z = a$, and then the order of refractive-index magnitudes is given by $n_x < n_y < n_z$ [14]. Note the c -axis is set to be parallel to the x -axis. A schematic diagram showing the definition of the optical and crystallographic axes in the spherical coordinate is shown in Figure 1b, where a wave vector representing the direction of beam propagation is also defined as:

$$\vec{k} = (\sin \theta \cos \phi, \sin \theta \sin \phi, \cos \theta) \quad (1)$$

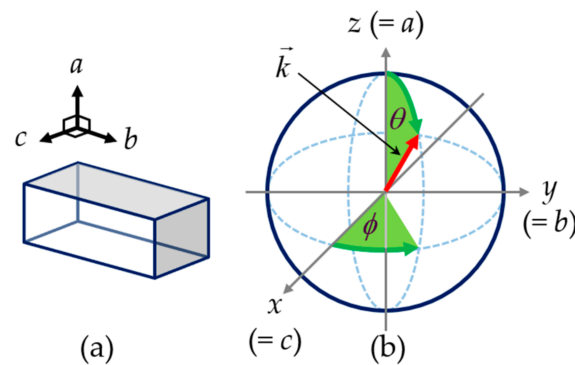


Figure 1. (a) A unit cell of $Pna2_1$ -BMBF crystal with a point symmetry of orthorhombic $mm2$. a , b , and c denote the crystallographic axes, and they are all perpendicular to each other. (b) A schematic diagram showing the definition of the crystallographic and optical axes in a spherical coordinate, where the wave vector (\vec{k}) representing the direction of beam propagation is also defined. ϕ and θ are the azimuthal and polar angles, respectively.

Here, ϕ and θ are the azimuthal and polar angles, respectively. When light is incident into a BMBF crystal, the refractive indices (RI's) of two eigen-polarization modes for the given \vec{k} -direction can be obtained by solving the Fresnel equation of the wave normal as follows [21],

$$n_{q\omega}^{(p)} = \sqrt{\frac{2}{-B_q \pm \sqrt{B_q^2 - 4C_q}}} \quad (2)$$

where the definitions of parameters are:

$$B_q = -k_x^2(b_q + c_q) - k_y^2(a_q + c_q) - k_z^2(b_q + a_q) \quad (3)$$

$$C_q = k_x^2 b_q c_q + k_y^2 a_q c_q + b_q a_q k_z^2 \quad (4)$$

$$a_q = n_{q\omega,x}, \quad b_q = n_{q\omega,y}, \quad c_q = n_{q\omega,z} \quad (5)$$

Here, q can be 1 or 2, then in the frequency-degenerate SPDC process, $n_{2\omega}$ and n_ω represent the RI's of pump photon with the frequency 2ω and signal and idler photons with the same frequency ω , respectively. k_x , k_y , and k_z in Equations (3) and (4) are defined in Equation (1). p in Equation (2) can be h or l , representing high or low RI. Each of these corresponds to when taking minus and plus in the \pm symbol of the denominator in Equation (2). The RI's of $Pna2_1$ -BMBF (i.e., n_x , n_y , and n_z) in Equation (5) are found in Ref. [14]. In the BMBF, two types of PM are possible for the SPDC process, i.e., Type I and Type II, where an input single photon (pump) with a frequency of 2ω generates a pair of

photons (signal and idler) with identical frequencies of ω that are parallel (for Type I) or orthogonally (for Type II) polarized to each other. The PM condition between pump, signal, and idler photons is given by $\vec{k}_{pump} = \vec{k}_{signal} + \vec{k}_{idler}$, and is classified into two types as follows:

$$n_{2\omega}^{(l)} = n_{\omega}^{(h)} \quad (\text{for Type I}) \tag{6}$$

$$2n_{2\omega}^{(l)} = n_{\omega}^{(h)} + n_{\omega}^{(l)} \quad (\text{for Type II}) \tag{7}$$

When photons of different frequencies pass through a BMBF crystal, temporal walk-off (ΔT) between interacting photons occurs due to their difference in GV. This GV mismatch is defined as ΔT per unit crystal length as follows,

$$\frac{\Delta T}{L} = \frac{\Delta n_g}{c}, \tag{8}$$

where, L, c and Δn_g represent the crystal length, the speed of light in vacuum, and the group index difference between interacting photons, respectively. So, when $\Delta n_g = 0$, the GV matching is satisfied, and for each type, it can be expressed as:

$$n_{g,2\omega}^{(l)} = n_{g,\omega}^{(h)} \quad (\text{for Type I}) \tag{9}$$

$$2n_{g,2\omega}^{(l)} = n_{g,\omega}^{(h)} + n_{g,\omega}^{(l)} \quad (\text{for Type II}) \tag{10}$$

Then, the two types of EPM conditions are defined as when Equations (6) and (9) (for Type I), or Equations (7) and (10) (for Type II) are satisfied simultaneously. Each of the equations is a 3-variable function for pump wavelength (λ_p), θ , and ϕ , so by solving a system of equations (i.e., Equations (6) and (9), or Equations (7) and (10)) for a given λ_p , we can find a set of θ and ϕ , i.e., the direction of \vec{k} . Thus, by sweeping \vec{k} in the range of directions where the set of solutions exists, it is possible to continuously tune the resonant wavelength of the pump that produces pure biphoton-states. In contrast, for uniaxial crystals, \vec{k} is a 1-variable function of the angle (say, θ). Therefore, the PM and GV matching conditions are given as a 2-variable function of λ_p and θ , so they can have only one set of solutions of λ_p and θ . In other words, in uniaxial crystals, at most only one \vec{k} -direction can satisfy the EPM condition for a given wavelength. So, the SPDC using the EPM scheme in uniaxial crystals requires more tricky optical alignment than in biaxial crystals. For example, a pump laser with the exact EPM wavelength is required, and the beam must be aligned along the exact PM direction of the uniaxial crystal in experiments. In reality, however, the optical properties of the crystal depend on the manufacturer, so both θ for EPM and the corresponding λ_p also vary slightly. In contrast, in the case of biaxial crystals, λ_p for EPM can always be found for the given \vec{k} -direction in the range where the solution sets exist.

The BMBF is a biaxial birefringent crystal with a point symmetry mm2, and the crystallographic axes and the optical axes have the relationships of $x = c, y = b$, and $z = a$. In this case, the effective nonlinearity for a given \vec{k} -direction is defined as [22],

$$d_{eff}^{(i)} = \xi_{i1}d_{15} + \xi_{i2}d_{24} + \xi_{i3}d_{31} + \xi_{i4}d_{32} + \xi_{i5}d_{33} \tag{11}$$

where the nonlinear optic coefficients are $d_{15} = d_{31} = 0.09$ pm/V, $d_{24} = d_{32} = -0.39$ pm/V, and $d_{33} = 0.51$ pm/V when Kleinman symmetry conditions are valid [14]. The subscript i in Equation (11) can be 1 or 2, and represents Type I and Type II, respectively. Then the ξ -coefficients for each type are given as:

$$\begin{aligned}
 \xi_{11} &= -2A^2EH(BGH - CE) \\
 \xi_{12} &= -2(BCE - GH)(BGH - CE)(BCH + EG) \\
 \xi_{13} &= -A^2H^2(BEG + CH) \\
 \xi_{14} &= -(BCH + EG)^2(BEG + CH) \\
 \xi_{15} &= -(BGH - CE)^2(BEG + CH)
 \end{aligned}
 \tag{12}$$

$$\begin{aligned}
 \xi_{21} &= A^2E^2(BGH - CE) + A^2EH(BEG + CH) \\
 \xi_{22} &= (BCE - GH)^2(BGH - CE) + (BCE - GH)(BCH + EG)(BEG + CH) \\
 \xi_{23} &= A^2EH(BEG + CH) \\
 \xi_{24} &= (BCE - GH)(BCH + EG)(BEG + CH) \\
 \xi_{25} &= (BGH - CE)(BEG + CH)^2
 \end{aligned}
 \tag{13}$$

Here, the angle-dependent parameters of $A, B, C, G, E,$ and H are given by $\sin\theta, \cos\theta, \sin\phi, \cos\phi, \sin\delta,$ and $\cos\delta,$ respectively. θ and ϕ are defined in Figure 1b. δ is the angle introduced only for convenience and is defined as:

$$\tan \delta \equiv \frac{2BCG}{A^2 \cot^2 V_z + C^2 - B^2G^2}
 \tag{14}$$

where V_z represents the angle between the z -axis and the optic axis of biaxial birefringence when the relation of $n_x < n_y < n_z$ is valid, as in the case of the BMBF crystal. V_z is related to Sellmeier equations of the crystal, and thus is wavelength-dependent. Therefore, $d_{eff}^{(i)}$ is also a 3-variable function for $\lambda_p, \theta,$ and $\phi,$ so the effective nonlinearity of each type can be obtained by substituting the solution sets of $\lambda_p, \theta,$ and ϕ that satisfy the corresponding EPM types. The SPDC efficiency is proportional to the square of the d_{eff} coefficient for a given \vec{k} -direction [23].

When the interacting beams pass through a birefringent crystal, the spatial walk-off between the beams occurs due to the difference between the direction of beam propagation (\vec{k}) and the direction of energy flow (Poynting vector, \vec{s}), as well as due to the birefringence. Here, the angle $\rho_q^{(p)}$ between \vec{s} and \vec{k} is given by,

$$\tan \rho_q^{(p)} \equiv \left\{ n_{q\omega}^{(p)} \right\}^2 \left[\left(\frac{k_x}{\left\{ n_{q\omega}^{(p)} \right\}^{-2} - a_q} \right)^2 + \left(\frac{k_y}{\left\{ n_{q\omega}^{(p)} \right\}^{-2} - b_q} \right)^2 + \left(\frac{k_z}{\left\{ n_{q\omega}^{(p)} \right\}^{-2} - c_q} \right)^2 \right]^{-1/2}
 \tag{15}$$

where all parameters of Equation (15) are defined in Equations (1)–(5) [21]. As discussed earlier in Equation (6), for Type I EPM, the pump photon with a low RI interacts with the high RI signal and idler photons with the same polarization state. In this case, the walk-off can be defined as the angle (w) between the Poynting vectors of the interacting photons, and is given as [24],

$$\cos w = \cos \rho_1^{(h)} \cos \rho_2^{(l)}
 \tag{16}$$

In the case of Type II EPM described by Equation (7), the walk-off angle w is defined as the largest angle formed by the interacting beams. Since the low RI signal (or idler) beam ($\rho_1^{(l)}$) is always placed between the low RI pump beam ($\rho_2^{(l)}$) and the high RI idler (or signal) beam ($\rho_1^{(h)}$), w for Type II can use the same definition as for Type I in Equation (16). As can be seen from Equation (15), w is also the 3-variable function for $\lambda_p, \theta,$ and $\phi,$ so w of each type can be obtained by substituting the set of solutions of $\lambda_p, \theta,$ and ϕ that satisfy the corresponding EPM types. Note that even with the same definition of $w,$ the calculation result is different for each type because the solution sets of $\lambda_p, \theta,$

and ϕ depend on the EPM type. The maximum deviation between the interacting beams after passing through a crystal of length L can be expressed as:

$$\Delta = L \tan \omega \quad (17)$$

The construction of the signal-idler JSA and the calculation of the purity of biphoton state via Schmidt decomposition is a good way to quantify the heralded-state spectral purity of SPDC output. The biphoton state $|\psi\rangle$ generated from SPDC can be expressed as [25],

$$|\psi\rangle = \int_0^\infty \int_0^\infty d\omega_s d\omega_i f(\omega_s, \omega_i) \hat{a}_s^\dagger(\omega_s) \hat{a}_i^\dagger(\omega_i) |0\rangle |0\rangle \quad (18)$$

where, \hat{a}_s^\dagger and \hat{a}_i^\dagger denote the creation operators of the signal and idler photons, respectively, and ω_s and ω_i are the corresponding frequencies. Here, the normalized correlation function $f(\omega_s, \omega_i)$, representing the biphoton JSA, is expressed as the product of pump envelop function and the PM function as follows:

$$f(\omega_s, \omega_i) = \alpha(\omega_s, \omega_i) \varphi(\omega_s, \omega_i) \quad (19)$$

Assuming a pump with Gaussian spectral shape, the pump envelope (PE) function can be written as,

$$\alpha(\omega_s, \omega_i) = \exp\left[-\frac{(\omega_s + \omega_i - \omega_p)^2}{\sigma_p^2}\right] \quad (20)$$

where ω_p and σ_p represent the center frequency and bandwidth of the pump, respectively. The PM function is given in the form of a sinc-function as shown below,

$$\varphi(\omega_s, \omega_i) \propto \text{sinc}\left(\frac{\Delta k L}{2}\right) \quad (21)$$

where L and Δk are the crystal length and the phase mismatch defined as $\Delta k = \vec{k}_p - \vec{k}_s - \vec{k}_i$, respectively [23]. For the given \vec{k} -direction (i.e., θ and ϕ) that satisfies each type of EPM, Equation (19) is given as a function of the signal and idler wavelengths (or λ_s and λ_i), so the JSA can be plotted on a two-dimensional plane as a function of λ_s and λ_i . The purity can be calculated via the following Schmidt decomposition,

$$f(\omega_s, \omega_i) = \sum_j \sqrt{c_j} |\zeta_{s,j}\rangle |\zeta_{i,j}\rangle \quad (22)$$

where Schmidt coefficients, c_j , denote a set of non-negative real numbers satisfying the normalization condition, $\sum_j c_j = 1$. $|\zeta_{s,j}\rangle$ and $|\zeta_{i,j}\rangle$ represent the orthonormal basis states (i.e., Schmidt modes), respectively. Then the purity, p , is defined as the sum of squares of Schmidt coefficients as [25]:

$$p = \sum_j c_j^2 \quad (23)$$

So, once we plot the JSA as a function of λ_s and λ_i in a 2-dimensional plane, p can be calculated via the Schmidt decomposition in Equation (22).

3. Simulations and Discussion

Figure 2 shows the numerical simulation results of the PM and GV matchings for Type I (Figure 2a–f) and Type II (Figure 2g–k). In each graph, the dotted and solid lines indicate the \vec{k} -directions (θ and ϕ) that satisfy the PM and GV matching conditions for a given pump wavelength, respectively. The PM and GV matching curves were obtained by calculating Equations (6) and (9) (for Type I), or Equations (7)

and (10) (for Type II). The intersection point of each graph means the \vec{k} -direction satisfying the EPM, and appears over a wide wavelength range as expected in Section 2.

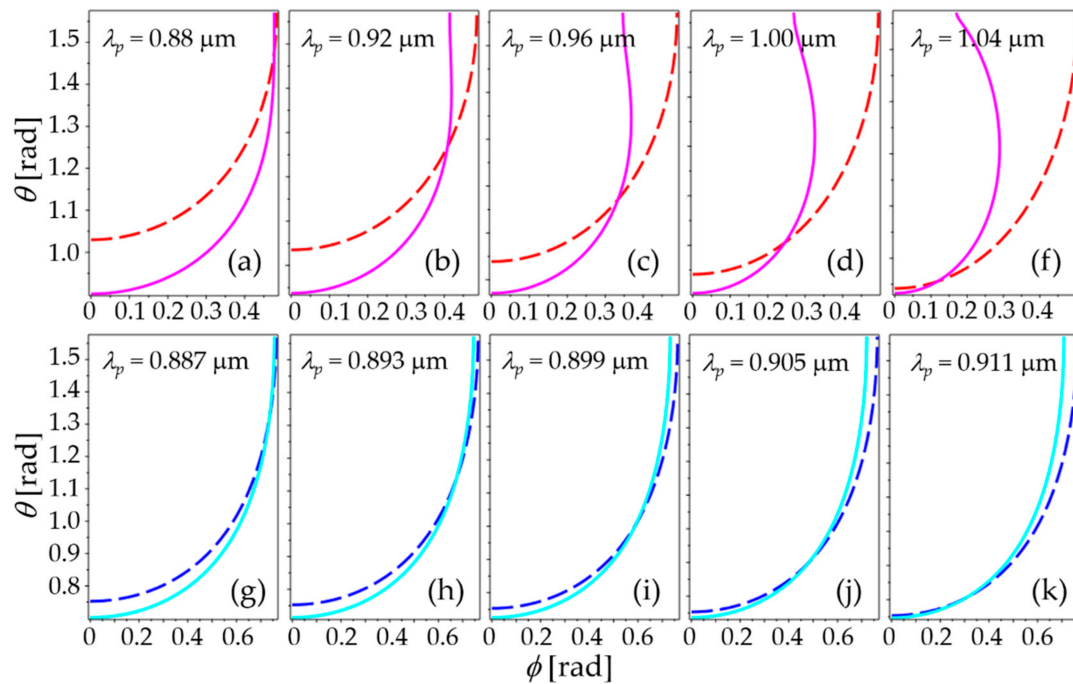


Figure 2. Numerical simulation results of the PM and GV matchings for Type I (a–f) and Type II (g–k). In each graph, the dotted and solid lines indicate the \vec{k} -directions (θ and ϕ) that satisfy the PM and GV matching conditions for a given pump wavelength, respectively.

Figure 3a shows the variation of the resonance pump wavelength (λ_p) satisfying each type of EPM while sweeping \vec{k} in space. Under each EPM condition, λ_p spans 876.15 nm to 1052.77 nm for Type I, and 883.92 nm to 914.33 nm for Type II. So, λ_p , which produces pure biphoton-states, can be continuously tuned by sweeping \vec{k} in those ranges. The \vec{k} -directions for the given EPM pump wavelength are plotted in Figure 3b (for Type I) and Figure 3c (for Type II) as a function of θ and ϕ . As plotted in Figure 3b,c, for both types, \vec{k} overall deviates more from the z-axis at shorter wavelengths.

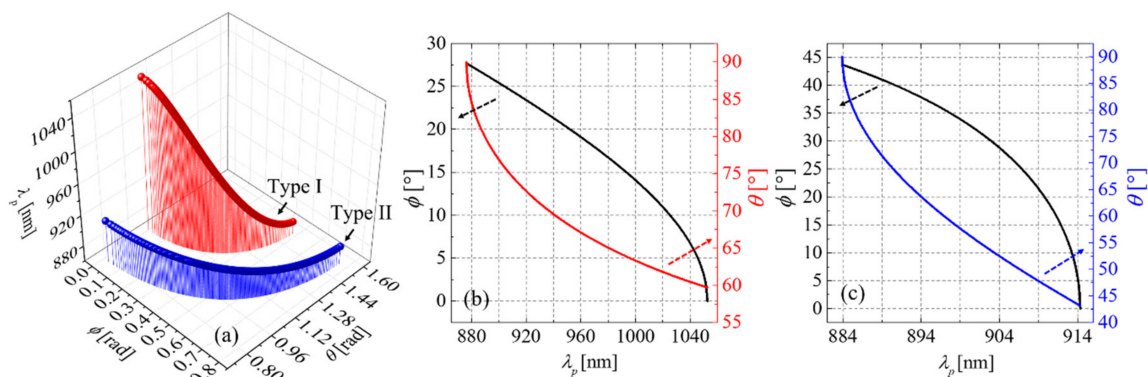


Figure 3. (a) Variation of the resonance pump wavelength (λ_p) satisfying each type of EPM while sweeping the k in space. The k -directions for a given EPM pump wavelength plotted as a function of θ and ϕ : (b) Type I, (c) Type II.

In order to find the \vec{k} -direction for higher SPDC efficiency, we now discuss the effective nonlinearity of each EPM type. The effective nonlinear optic coefficients (d_{eff}) are calculated numerically using Equation (11), the results are plotted in Figure 4a (for Type I) and Figure 4b (for Type II) as a function of λ_p . Here, each λ_p value is taken from the results in Figure 3a, and corresponds to the EPM wavelength for the given \vec{k} -direction. In Figure 4a, the magnitude of d_{eff} has maximum values at 914.3 nm and 1023.9 nm for Type I. For Type II, d_{eff} values peak at 887.1 nm, 904.4 nm, and 914.33 nm, in particular the last one denotes when $\phi = 0$, i.e., when \vec{k} lies on the x - z plane. The value of d_{eff} at 914.33 nm is calculated to 0.28 pm/V for Type II, which is due to the large contribution of term $\xi_{22}d_{24}$ in Equation (11) for a given \vec{k} -direction. The maximum walk-off angles (w), calculated using Equation (16) under EPM, are plotted in Figure 5a (for Type I) and Figure 5b (for Type II) as a function of the EPM λ_p . Over the whole range of λ_p , the calculated w spans 1.23° – 1.36° for Type I and 1.47° – 1.53° for Type II. The corresponding deviations (Δ) of the interacting beams per unit crystal of length are about $23 \mu\text{m}/\text{mm}$ and $26 \mu\text{m}/\text{mm}$, which can be sufficiently overcome by using a pump beam of a larger size in thick crystals. The EPM λ_p for each peak d_{eff} shown in Figure 4, \vec{k} -direction in terms of θ and ϕ , the corresponding d_{eff} , w , and Δ are summarized in Table 1.

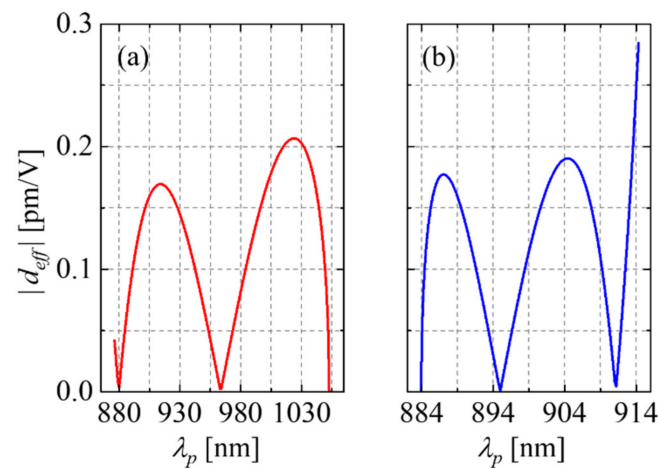


Figure 4. Effective nonlinear optic coefficients (d_{eff}) for (a) Type I and (b) Type II calculated numerically under the EPM conditions.

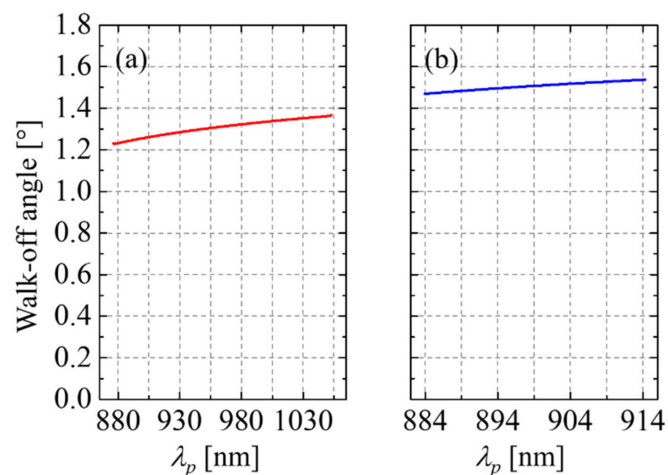


Figure 5. Maximum walk-off angle (w) of the interacting beams for (a) Type I and (b) Type II calculated numerically under the EPM conditions.

Table 1. Type I and Type II EPM: the resonant pump wavelength (λ_p), k -directions (i.e., θ and ϕ), the effective nonlinear optic coefficient (d_{eff}), the walk-off angle (w), and the beam deviation (Δ).

	Case	λ_p [nm]	ϕ [°]	θ [°]	d_{eff} [pm/V]	w [°]	Δ [$\mu\text{m}/\text{mm}$]
Type I	(1)	914.0	24.01	73.78	0.17	1.27	22.2
	(2)	1023.9	10.28	61.54	0.21	1.35	23.5
Type II	(3)	887.1	42.07	75.29	0.18	1.48	25.8
	(4)	904.4	28.33	52.11	0.19	1.52	26.5
	(5)	914.33	0	43.16	0.28	1.54	26.8

In order to quantify the heralded-state spectral purity of SPDC output, we now analyze the signal-idler JSA properties and calculate the purity of biphoton state. Figure 6 shows the joint spectral properties of the case (5) in Table 1, i.e., Type II SPDC with the highest d_{eff} . Note that in this case \vec{k} lies on the x - z plane (i.e., $\phi = 0$ in Figure 1b), so the optical alignment is relatively easy compared to the other cases in Table 1. The density plot of PM function shows typical EPM characteristics as in the case of the collinear, i.e., $+45^\circ$, as plotted in Figure 6a. The joint spectral intensity (JSI) calculated for the 8-nm bandwidth PE function (Figure 6b) is plotted in Figure 6c. Here, the JSI is defined as $|JSA|^2$. The solid and dashed lines in Figure 6d represent the contour lines for JSI = 0.5 and a circle with a diameter of 27 nm, respectively. The contour line shows a circular shape, and the purity calculated using Schmidt decomposition in Equation (22) is as high as 0.997. Figure 7 shows the JSI properties of cases (3) and (4) in Table 1, where the PE functions of 5.2-nm and 7-nm bandwidth, respectively, were considered for higher purity. All results shown in Figures 6 and 7 are calculated for a crystal length of 10 mm. The calculated JSI's are plotted in Figure 7a (for the case (3)) and Figure 7c (for the case (4)). The contours of JSI = 0.5 shown in Figure 7b,d exhibit circular shapes, and their diameters are 17.5 nm and 23 nm, respectively. The calculated spectral purity is as high as 0.997 for both cases.

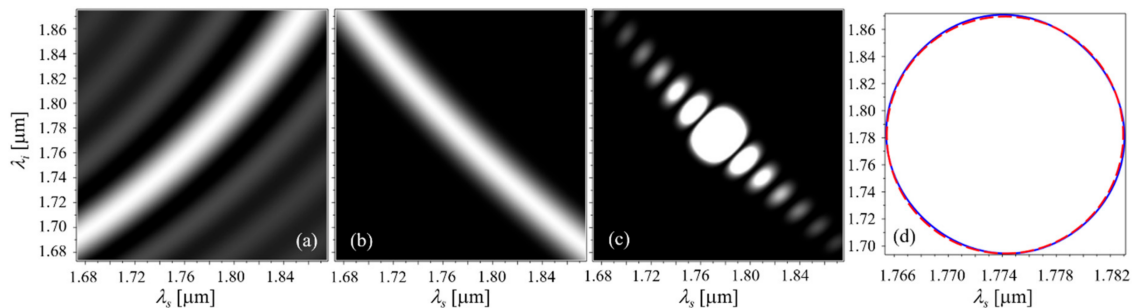


Figure 6. For Type II case (5) in Table 1: (a) PM function, (b) Pump envelop function, (c) JSI, and (d) the contour line for JSI = 0.5 (solid line) shown with a circle with a diameter of 27 nm (dashed line). The calculated purity is 0.997.

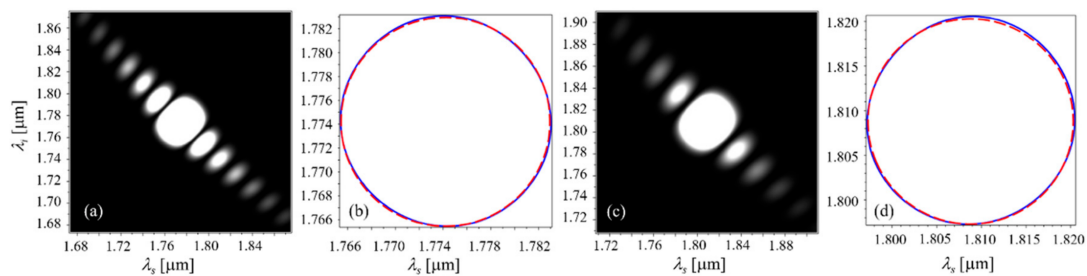


Figure 7. Type II case (3) in Table 1: (a) JSI, (b) the contour line for JSI = 0.5 (solid line) and a circle with a diameter of 17.5 nm (dashed line); Type II case (4) in Table 1: (c) JSI, (d) the contour line for JSI = 0.5 (solid line) and a circle with a diameter of 23 nm (dashed line). The calculated purity is 0.997 for both cases.

For the Type I cases of (1) and (2) in Table 1, the JSI's show large, localized shapes around their SPDC resonances, as shown in Figure 8a,b, without pump filtering. The calculated purities remain high as 0.726 and 0.833, respectively, even without pump filtering. The contours of JSI = 0.5 are plotted in Figure 8c (for the case (1)) and Figure 8d (for the case (2)), where the red long-dashed, magenta dotted, green dashed, blue dash-dotted, and cyan solid lines represent the results calculated for crystals of length 10, 20, 30, 40, and 50 mm, respectively. Since the resonance spectrum is inversely proportional to the crystal length, the area inside the contour line decreases as the crystal length increases, but the localized spectral shapes centered on the resonance point are maintained, as shown in Figure 8c,d.

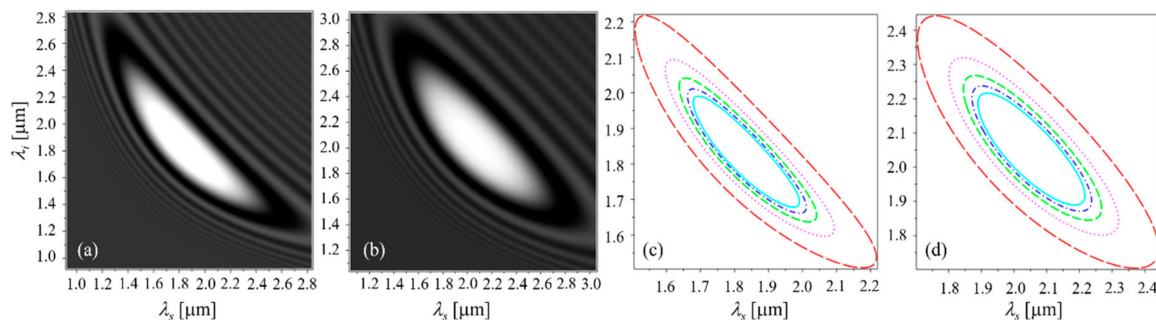


Figure 8. JSI without pump filtering for Type I (a) case (1), (b) case (2); the contour line of JSI = 0.5 (c) case (1), (d) case (2). The crystal lengths used in the simulation are 10, 20, 30, 40, 50 mm in order of decreasing the area inside the contour.

The entangled photon-pairs generated by the EPM SPDC in a $Pna2_1$ -BMBF crystal have their resonances in a broad spectral range, and the calculation results show that quantum signal processing is feasible by choosing the spectral region of the photon-pairs within $2\ \mu\text{m}$. Since silica-based fibers still have transparency in this spectral region (e.g., silica fiber SM2000, Thorlabs, Newton, NJ, USA), we expect our research to provide flexibility and diversity in experimental quantum information processing using fiber-optic transmission lines, as well as free space quantum communication.

4. Conclusions

We have theoretically and numerically investigated the entangled photon-pair generation in a newly developed borate crystal, $Pna2_1$ -BMBF. The SPDC based on the EPM scheme in bulk, mm² biaxial crystals was first described theoretically, which was applied to the case of $Pna2_1$ -BMBF. The heralded-state spectral purity of SPDC output was quantified via JSA analyses, and the results show that the maximum purity calculated for Type II EPM with a proper pump filtering is as high as 0.997. For Type I EPM, the JSI shows a large localized shape and the calculated purity reaches 0.833 even without pump filtering. The spectral position of the photon-pairs produced by the EPM SPDC in a BMBF crystal can be chosen over the broad range of $<2\ \mu\text{m}$, which is still within the silica fiber transparency. Our studies have shown that BMBF has the following advantages over other borate crystals such as BBO and BiBO, which are commonly used for photon pair generation: First, in BMBF, the photon pair spectrum can be selected or tuned over a wide spectral range of interest, whereas BBO is a uniaxial crystal where only one Type II EPM resonance exists. In addition, BBO is highly hygroscopic and requires strict control of experimental conditions. However, BMBF is advantageous for packaging due to its low hygroscopicity and high laser damage threshold, so it can be used as a quantum light source platform even outside the laboratory. Since BiBO has a monoclinic (point group 2) crystal structure, the crystallographic axes are not perpendicular to each other and thus deviated from the optical axes. Thus, non-collinear vector PM is required, resulting in the large spatial walk-off between the interacting beams. The walk-off angle calculated for BiBO is 40.7 mrad (i.e., 2.31°), which is 1.5 times larger than the largest walk-off angle in the case presented in this paper [26]. Thus, in the case of BiBO, the length of the crystal that can be used in the SPDC experiment is limited to being shorter

than in the case of BMBF. Our research is expected to provide flexibility in experimental quantum information processing, such as fiber-optic and free space quantum communication.

Author Contributions: Conceptualization, K.J.L.; Simulation, D.L. and K.J.L.; writing—original draft preparation, D.L. and I.K.; writing—review and editing, I.K. and K.J.L.; supervision, K.J.L. All authors have read and agreed to the published version of the manuscript.

Funding: This research was funded by National Research Foundation of Korea (Grant NRF-2019R1F1A1063937 and in Korea Institute of Science and Technology (KIST) (Grant 2E29580-19-147).

Conflicts of Interest: The authors declare no conflict of interest.

References

1. Bouwmeester, D.; Weinfurter, H.; Zeilinger, A. *The Physics of Quantum Information*; Springer: Berlin/Heidelberg, Germany, 2001; pp. 49–92.
2. Burnham, D.C.; Weinberg, D.L. Observation of simultaneity in parametric production of optical photon pairs. *Phys. Rev. Lett.* **1970**, *25*, 84–87. [[CrossRef](#)]
3. Kwiat, P.G.; Mattle, K.; Weinfurter, H.; Zeilinger, A.; Sergienko, A.V.; Shih, Y. New high-intensity source of polarization-entangled photon pairs. *Phys. Rev. Lett.* **1995**, *75*, 4337–4342. [[CrossRef](#)] [[PubMed](#)]
4. Mosley, P.J.; Lundeen, J.S.; Smith, B.J.; Wasylczyk, P.; U'Ren, A.B.; Silberhorn, C.; Walmsley, I.A. Heralded generation of ultrafast single photons in pure quantum states. *Phys. Rev. Lett.* **2008**, *100*, 133601. [[CrossRef](#)] [[PubMed](#)]
5. Bock, M.; Lenhard, A.; Chunnillal, C.; Becher, C. Highly efficient heralded single-photon source for telecom wavelengths based on a PPLN waveguide. *Opt. Express* **2016**, *24*, 23992–24001. [[CrossRef](#)] [[PubMed](#)]
6. Halevy, A.; Megidish, E.; Dovrat, L.; Eisenberg, H.S.; Becker, P.; Bohatý, L. The biaxial nonlinear crystal BiB₃O₆ as a polarization entangled photon source using non-collinear type-II parametric down-conversion. *Opt. Express* **2011**, *19*, 20420–20434. [[CrossRef](#)] [[PubMed](#)]
7. Chen, L.-K.; Li, Z.-D.; Yao, X.-C.; Huang, M.; Li, W.; Lu, H.; Yuan, X.; Zhang, Y.-B.; Jiang, X.; Peng, C.-Z.; et al. Observation of ten-photon entanglement using thin BiB₃O₆ crystals. *Optica* **2017**, *4*, 77–83. [[CrossRef](#)]
8. Fedrizzi, A.; Herbst, T.; Poppe, A.; Jennewein, T.; Zeilinger, A. A wavelength-tunable fiber-coupled source of narrowband entangled photons. *Opt. Express* **2007**, *15*, 15377–15386. [[CrossRef](#)] [[PubMed](#)]
9. Steinlechner, F.; Gilaberte, M.; Jofre, M.; Scheidl, T.; Torres, J.P.; Pruneri, V.; Ursin, R. Efficient heralding of polarization-entangled photons from type-0 and type-II spontaneous parametric downconversion in periodically poled KTiOPO₄. *J. Opt. Soc. Am. B* **2014**, *31*, 2068–2076. [[CrossRef](#)]
10. Kim, T.; Fiorentino, M.; Wong, F.N.C. Phase-stable source of polarization-entangled photons using a polarization Sagnac interferometer. *Phys. Rev. A* **2006**, *73*, 012316. [[CrossRef](#)]
11. Kuzucu, O.; Wong, F.N.C. Pulsed Sagnac source of narrow-band polarization-entangled photons. *Phys. Rev. A* **2008**, *77*, 032314. [[CrossRef](#)]
12. Predojevic, A.; Grabher, S.; Weihs, G. Pulsed Sagnac source of polarization entangled photon pairs. *Opt. Express* **2012**, *20*, 25022–25029. [[CrossRef](#)] [[PubMed](#)]
13. Chen, C.; Sasaki, T.; Li, R.; Wu, Y.; Lin, Z.; Mori, Y.; Hu, Z.; Wang, J.; Uda, S.; Yoshimura, M.; et al. *Nonlinear Optical Borate Crystals: Principles and Applications*; Wiley-VCH Verlag & Co. KGaA: Weinheim, Germany, 2012; pp. 117–260.
14. Mutailipu, M.; Zhang, M.; Wu, H.; Yang, Z.; Shen, Y.; Sun, J.; Pan, S. Ba₃Mg₃(BO₃)₃F₃ polymorphs with reversible phase transition and high performances as ultraviolet nonlinear optical materials. *Nat. Comm.* **2018**, *9*, 3089. [[CrossRef](#)] [[PubMed](#)]
15. Giovannetti, V.; Maccone, L.; Shapiro, J.H.; Wong, F.N.C. Generating entangled two-photon states with coincident frequencies. *Phys. Rev. Lett.* **2002**, *88*, 183602. [[CrossRef](#)] [[PubMed](#)]
16. Giovannetti, V.; Maccone, L.; Shapiro, J.H.; Wong, F.N.C. Extended phase-matching conditions for improved entanglement generation. *Phys. Rev. A* **2002**, *66*, 043813. [[CrossRef](#)]
17. Raicol Crystals Ltd. Available online: <https://raicol.com> (accessed on 29 October 2020).
18. Jin, R.-B.; Shimizu, R.; Wakui, K.; Fujiwara, M.; Yamashita, T.; Miki, S.; Terai, H.; Wang, Z.; Sasaki, M. Pulsed Sagnac polarization-entangled photon source with a PPKTP crystal at telecom wavelength. *Opt. Express* **2014**, *22*, 11498–11507. [[CrossRef](#)] [[PubMed](#)]

19. Li, Y.; Zhou, Z.-Y.; Ding, D.-S.; Shi, B.-S. CW-pumped telecom band polarization entangled photon pair generation in a Sagnac interferometer. *Opt. Express* **2015**, *23*, 28792–28800. [[CrossRef](#)] [[PubMed](#)]
20. Lee, K.J.; Lee, S.; Shin, H. Extended phase-matching properties of periodically poled potassium niobate crystals for mid-infrared polarization-entangled photon-pair generation. *Appl. Opt.* **2016**, *55*, 9791–9796. [[CrossRef](#)] [[PubMed](#)]
21. Yariv, A.; Yeh, P. *Photonics: Optical Electronics in Modern Communications*, 6th ed.; Oxford University Press: New York, NY, USA, 2007; pp. 30–33.
22. Dmitriev, V.G.; Nikogosyan, D.N. Effective nonlinearity coefficients for three-wave interactions in biaxial crystals of mm2 point group symmetry. *Opt. Comm.* **1993**, *95*, 173–182. [[CrossRef](#)]
23. Boyd, R.W. *Nonlinear Optics*, 4th ed.; Academic Press: San Diego, CA, USA, 2020; pp. 70–73.
24. Brehat, F.; Wyncke, B. Calculation of double-refraction walk-off angle along the phase-matching directions in nonlinear biaxial crystals. *J. Phys. B At. Mol. Opt. Phys.* **1989**, *22*, 1891–1898. [[CrossRef](#)]
25. Mosley, P.J.; Lundeen, J.S.; Smith, B.J.; Walmsley, I.A. Conditional preparation of single photons using parametric downconversion: A recipe for purity. *New J. Phys.* **2008**, *10*, 093011. [[CrossRef](#)]
26. Red Optronics. Available online: <http://www.redoptronics.com/BIBO-crystal.html> (accessed on 16 December 2020).

Publisher's Note: MDPI stays neutral with regard to jurisdictional claims in published maps and institutional affiliations.



© 2020 by the authors. Licensee MDPI, Basel, Switzerland. This article is an open access article distributed under the terms and conditions of the Creative Commons Attribution (CC BY) license (<http://creativecommons.org/licenses/by/4.0/>).